THE ASTROPHYSICAL JOURNAL, 647:1452–1465, 2006 August 20

NONTHERMAL SPECTRAL LINE BROADENING AND THE NANOFLARE MODEL

S. PATSOURAKOS[1] AND J. A. KLIMCHUK
Space Science Division, Naval Research Laboratory, 4555 Overlook Avenue SW, Washington, DC 20375; patsourakos@nrl.navy.mil
Received 2005 March 30; accepted 2006 April 27

ABSTRACT

A number of theoretical and observational considerations suggest that coronal loops are bundles of unresolved, impulsively heated strands. This "nanoflare" model, as it is sometimes called, predicts high-speed evaporative upflows, which might be revealed as nonthermal broadening of spectral line profiles. We have therefore generated synthetic line profile observations based on one-dimensional hydrodynamic simulations for comparison with actual observations. The predicted profiles for Ne VIII (770.4 Å), a transition region line, and Mg X (624.9 Å), a warm coronal line, have modest broadening that agrees well with existing observations. The predicted profiles for Fe XVII (254.87 Å), a hot line that will be observed by the Extreme Ultraviolet Imaging Spectrometer (EIS) on the *Solar-B* mission, are somewhat broader and are also consistent with the limited number of hot line observations that are currently available. Moreover, depending on the properties of the assumed nanoflare and other parameters of the simulation, the Fe XVII profile can have distinctive enhancements in the line wing. This indicates a powerful diagnostic capability that can be exploited once *Solar-B* is launched.

Subject headings: hydrodynamics — Sun: corona

Online material: color figures

1. INTRODUCTION

It is well known that spectral emission line profiles formed in the solar corona and transition region are considerably broader than expected on the basis of the thermal motions of the emitting ions. This nonthermal broadening has been measured in soft X-rays (SXRs), the ultraviolet, and the visible, and the implied velocities are generally in the range of 10–60 km s^{-1} for temperatures in the range 0.1–6 MK (e.g., Kjeldseth Moe & Nicolas 1977; Cheng et al. 1979; Hassler et al. 1990; Saba & Strong 1991; Dere & Mason 1993; Doyle et al. 1997; Sterling 1997; Erdélyi et al. 1998; Chae et al. 1998; Peter 1999; Teriaca et al. 1999; Brosius et al. 2000; Spadaro et al. 2000; Doschek & Feldman 2000; Peter 2001; Patsourakos & Vial 2000; Feldman et al. 2003; Landi et al. 2003; Singh et al. 2003; Marsch et al. 2004). Substantial nonthermal line broadening under coronal conditions is observed in other stars as well (e.g., Schmitt & Wichmann 2001; Young et al. 2001; Ayres et al. 2003; Redfield et al. 2003; Chung et al. 2004). There are a number of possible causes of the broadening, including turbulence and unresolved wave motions, but perhaps the most likely explanation is unresolved systematic motions of a non-oscillatory nature. The solar corona is known to be very dynamic. Field-aligned flows are easily generated by non-steady heating, and even by steady heating if the energy is distributed asymmetrically along a coronal flux tube (Mariska & Boris 1983; Patsourakos et al. 2004b) or highly concentrated near the footpoints (Serio et al. 1981; Karpen et al. 2001; Müller et al. 2004). Irrespective of their origin, nonthermal velocities place strong constraints on any heating mechanism that should be able to reproduce them (e.g., Zirker 1993).

We have argued that most coronal heating mechanisms are impulsive when examined from the perspective of elemental magnetic flux strands (Klimchuk 2006). We therefore favor the idea of nanoflares. Parker (1983, 1988) suggested that nanoflares may occur in coronal fields that become tangled by the random footpoint shuffling associated with photospheric convection. The magnetic stresses that build up must eventually be relieved, and the secondary instability is a very promising explanation for how this may take place (Dahlburg et al. 2003, 2005).

The concept of nanoflares has inspired a number of modeling efforts, beginning with Cargill (1994), that treat coronal loops as bundles of unresolved, impulsively heated strands (see references in Klimchuk 2006). These models are able to explain certain properties of observed loops that cannot be understood with steady heating, including the tendency for warm ($\sim$1 MK) loops to be overdense compared to static equilibrium and to have nearly constant temperatures as derived from filter ratios (Aschwanden et al. 1999; Lenz et al. 1999; Winebarger et al. 2003; Patsourakos et al. 2004b).

One fundamental property of impulsive heating is the production of high-speed chromospheric evaporation (Antiochos & Sturrock 1978; Pallavicini et al. 1983; Cheng et al. 1983). The abrupt temperature increase that results from sudden heating causes an intense heat flux into the transition region and the chromosphere. This drives an evaporative upflow with speeds that are often well in excess of 100 km s^{-1} in nanoflare simulations. Are upflows of this magnitude consistent with the observed nonthermal line broadening of only 10–60 km s^{-1}? If not, then the nanoflare idea must be seriously questioned. One major objective of our study is to answer this critical question. As we will show, there does indeed appear to be a consistency with existing observations. A second major objective of our study is to determine whether detailed line profile observations, especially those from future missions, can be used to diagnose the properties of nanoflares. We will demonstrate that profiles of very hot lines are expected to have distinctive signatures of the energy release.

Our approach to the problem is to use numerical simulations to generate synthetic line profiles corresponding to observations of unresolved bundles of loop strands. The strands are assumed to be heated impulsively, and their evolution is modeled with a powerful one-dimensional hydrodynamic simulation code. We make the additional assumption that the nanoflares occur randomly

[1] Also at: Center for Earth Observing and Space Research, School of Computational Sciences, George Mason University, 4400 University Drive, Fairfax, VA 22030.

over long periods of time so that we can approximate an instantaneous snapshot of the entire bundle by taking the time average of a single strand. We consider several different models: a base model and alternate models in which one or more of the base model parameters is modified. In this way we investigate the effects of the nanoflare magnitude and duration, the strand length, and the initial conditions.

From the models, we simulate observations in three different spectral lines: Ne VIII (770.4 Å), Mg X (624.9 Å), and Fe XVII (254.87 Å). These lines span a broad range of temperatures. In ionization equilibrium, their contribution functions peak at approximately 0.6, 1.2, and 5.0 MK, respectively. Ne VIII and Mg X have been well observed by several instruments, including the Coronal Diagnostics Spectrometer (CDS) on the *Solar and Heliospheric Observatory* (*SOHO*), and Fe XVII will be observed by the Extreme Ultraviolet Imaging Spectrometer (EIS) that will fly on the upcoming *Solar-B* mission. We measure a nonthermal velocity from each of the line profiles using the second moment technique.

Our paper is organized as follows. Section 2 describes the nanoflare simulations, the generation of synthetic line profiles, and the derivation of nonthermal velocities. Results are presented for the base model in § 3 and for the alternate models in § 4. Section 5 discusses actual observations of line profiles and published measurements of nonthermal velocities. Finally, § 6 summarizes our results and makes recommendations for future work.

2. NUMERICAL SIMULATIONS AND SPECTROSCOPY

We solve the time-dependent one-dimensional hydrodynamic equations using our state-of-the-art adaptively refined Godunov solver (ARGOS) code, described in detail in Antiochos et al. (1999). ARGOS employs the PARAMESH parallel adaptive mesh refinement (AMR) package, which dynamically refines or derefines the grid on the basis of the local density gradients. PARAMESH allows us to track the small spatial scales associated with nanoflare dynamics, including propagating shocks and moving transition regions.

During intense impulsive energy releases, such as nanoflares, the density increases much more slowly than the temperature. It is thus likely that the heat flux will saturate at a fraction of the free-streaming electron energy flux (e.g., Karpen & Devore 1987). As described in Patsourakos & Klimchuk (2005), we account for this saturation by expressing the heat flux as a combination of the classical (collisional) Spitzer-Harm heat flux and the saturated heat flux, assuring a smooth transition between the extreme cases with either classical or saturated heat flux dominating. Compressive viscosity is ignored in the base model, but is included in one of the alternate models.

We consider a semicircular strand with a constant cross section (e.g., Klimchuk 2000; López Fuentes et al. 2006). The base model (model 1) uses a total length of $L = 150$ Mm, which is typical of observed EUV loops (e.g., Aschwanden et al. 2000). Alternate model 7 uses a much shorter length of 60 Mm. In all cases the strand is assumed to lie in a vertical plane. Attached to each end of the coronal semicircle is a 60 Mm chromospheric section. We adopt a radiation loss function that decreases precipitously below $T = 3 \times 10^4$ K in order to maintain a nearly constant chromospheric temperature at this value. The simulation properly treats the transfer of mass between the chromosphere and corona (i.e., chromospheric evaporation and condensation), and it allows the top of the chromosphere to rise and fall in response to changes in the coronal pressure (Klimchuk 2006). The chromosphere is chosen to be many gravitational scale heights thick ($H_g \approx 1500$ km at $T = 3 \times 10^4$ K) so that the rigid wall boundary conditions at the base have negligible influence on the plasma dynamics and so that the thickness of the chromosphere is not affected by the depletion or accumulation of mass.

Each simulation begins with the plasma in static equilibrium. For the base model, a spatially uniform heating of $Q_0 = 3 \times 10^{-4}$ ergs cm^{-3} s^{-1} produces an initial apex temperature of $T_{0a} = 2.5$ MK and an initial apex density of $n_{0a} = 6 \times 10^8$ cm^{-3}. These conditions are similar to those predicted by the equilibrium scaling law theory of Rosner et al. (1978) and Serio et al. (1981). The background heating Q_0 is turned off when a far more intense nanoflare heating $Q_{\rm nano}$ is turned on, as described below.

We can interpret the initial state in two ways. First, it could correspond to a true static equilibrium that is maintained by a long-lived and steady heating that becomes disrupted by the nanoflare. Second, it could correspond approximately to a loop strand that is cooling after having been impulsively heated by an earlier nanoflare. In the absence of significant heating, all strands cool through a state in which the apex temperature and density take on the values of a static equilibrium (Winebarger & Warren 2004; Cargill & Klimchuk 2004). Because velocities are highly subsonic at this time, the entire strand is not far from static equilibrium conditions. Our simulation can therefore be interpreted as a cooling strand that is reheated when its apex temperature drops to 2.5 MK. Alternate models 5 and 6 begin with a cooler and more rarefied equilibrium for which $T_{0a} = 0.5$ MK and $n_{0a} = 7 \times 10^6$ cm^{-3}. This corresponds either to a much weaker prenanoflare heating or to a cooling strand that reaches lower temperatures before the next nanoflare occurs. Note that the temperature at which a cooling strand passes through equilibrium conditions depends on the nanoflare energy and other factors (Winebarger & Warren 2004; Cargill & Klimchuk 2004).

We impose a nanoflare energy release at time $t = 0$ s that has a spatially uniform heating rate $Q_{\rm nano} = 0.01$ ergs cm^{-3} s^{-1} and duration $\tau_{\rm nano} = 250$ s. This is similar to what would be expected from the secondary instability (Dahlburg et al. 2003, 2005). If the active region corona is completely filled with heated strands, then nanoflares of this magnitude must repeat once every few thousand seconds in each strand in order to satisfy the 10^7 ergs cm^{-2} s^{-1} observed energy flux requirements (Withbroe & Noyes 1977). This repetition interval is longer than a cooling time (e.g., Serio et al. 1991; Cargill et al. 1995), as our simulations will show, and therefore our assumed initial conditions are reasonable. If nanoflares repeated frequently, the plasma would be maintained quasi-statically at high temperatures (e.g., Kopp & Poletto 1993; Walsh et al. 1997; Mendoza-Briceño et al. 2002; Testa et al. 2005).

Note that the canonical nanoflare energy of $E_{\rm nano} \sim 10^{24}$ ergs suggested by Parker (1988) implies a strand diameter of 6×10^6 cm for our chosen value of $Q_{\rm nano}$. A loop with a diameter of 3×10^8 cm would therefore contain approximately 10^3 elemental strands. Also note that although our nanoflare produces a 10 MK peak temperature that is close to half that of a normal flare, the heating rate per unit volume is much less than that of a flare. To overcome the thermal conduction losses at the temperatures characteristic of flares would require a value of $Q_{\rm nano}$ that is at least an order of magnitude larger than what we have employed. (The conduction flux varies as $T^{7/2}/L$ in the classical regime.)

The solution of the hydrodynamic equations provides the distributions of density, temperature, and flow velocity along the strand as a function of time. From these, we generate synthetic spectral line profiles for Ne VIII (770.4 Å), Mg X (624.9 Å), and Fe XVII (254.87 Å). In ionization equilibrium, the $G(T)$ contribution functions of these lines exceed half-maximum in the approximate ranges 0.5–0.9 MK, 0.8–1.6 MK, and 3.0–7.0 MK, respectively. For multithermal plasmas with unknown temperature distributions, the contribution function weighted mean temperature $T_{G_{\rm mean}}$ is the best estimate of the temperature of the bulk of the plasma contributing to the line (Klimchuk & Cargill 2001). The quantity $T_{G_{\rm mean}}$ is $\approx$0.7, 1.3, and 5.1 MK for Ne VIII, Mg X, and Fe XVII, respectively. These values are slightly larger than the temperatures at which the contribution functions peak due to the existence of high-temperature tails in the functions.

The Fe XVII line will be observed by the EIS spectrometer on *Solar-B*. We originally considered the Ca XVII (192.82 Å) line, which will also be observed by EIS. It is much stronger than Fe XVII and is also formed near 5 MK, but it is blended with Fe XI (192.83 Å). It may be possible to remove the blend using a strong Fe XI line at 188 Å that shares the same upper level as the 192 Å line (G. Doschek 2005, private communication). For now, we feel it is safer to work with Fe XVII.

To synthesize the line profiles, we first compute the emissivity in each cell of the numerical grid:

$$\epsilon = n^2 G(T), \tag{1}$$

where n is the electron number density and $G(T)$ is the contribution function from version 4 of the CHIANTI atomic database package (Dere et al. 1997; Young et al. 2003). We then construct a Gaussian line profile for each cell, using a Doppler shift given by the line-of-sight velocity and a width given by the thermal broadening $(\lambda_0/c)(2kT/m)^{1/2}$, where m is the ion mass and λ_0 is the rest wavelength. In determining the Doppler shifts, we assume that the observations are made at disk center. This assumption tends to maximize the Doppler shifts, since the greatest velocities occur in the roughly vertical lower legs of the strand.

Because most reported observations of nonthermal line broadening tend to average over significant portions of active regions and/or the quiet Sun, we combine the line profiles from all the cells in the strand to obtain a spatially averaged profile. Some higher resolution observations are able to separate the coronal parts of loops from the transition region footpoints (which appear as "moss" in hot loops), so we also compute separate averages for a coronal section, which begins 10 Mm above the initial top of the chromosphere, and for the footpoint section below it. The footpoint section includes a small part of the lower corona in addition to the transition region. We would prefer to completely isolate the transition region, but this is difficult because the transition region moves up and down the strand in response to changes in the heating rate. It is not useful to define the transition region in terms of a fixed temperature range, because the temperature range of the steep gradient region depends strongly on the peak temperature in the corona, which is constantly changing.

As is done for real observations (e.g., Dere & Mason 1993), we measure the nonthermal velocities ξ of the profiles using the relationship

$$\Delta\lambda^2 = \frac{\lambda^2}{2c^2}\left(\frac{2kT_{G_{\rm mean}}}{m} + \xi^2\right), \tag{2}$$

where $\Delta\lambda^2$ is the second moment of the profile. Using the second moment rather than fitting the profiles with a given function (e.g., a Gaussian) has the advantage of not making any assumption about the form of the profiles. Nanoflares can give rise to rather complex line shapes, as we will show. Note that we use $T_{G_{\rm mean}}$ in equation (2), not the slightly different temperature at which $G(T)$ peaks. In the following we do not measure nonthermal velocities for profiles in which there are two clear components.

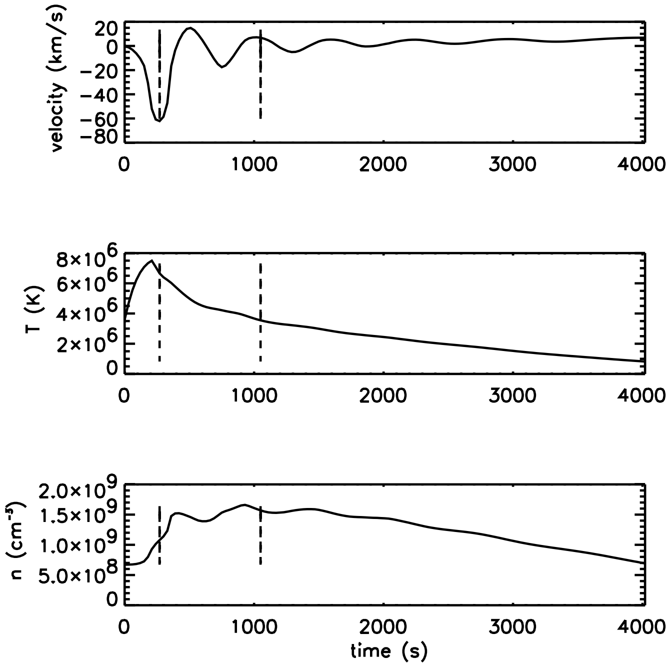

FIG. 1.—Evolution of velocity (*top*), temperature (*middle*), and density (*bottom*) halfway up the leg of the strand for the base model. Negative velocities correspond to upflows. The vertical dashed lines indicate the interval when the contribution function of the Fe XVII line is above half-maximum.

We remind the reader that plasma turbulence and MHD waves can contribute to nonthermal line broadening (e.g., Boland et al. 1975; Hassler et al. 1990; Dere & Mason 1993; Inverarity et al. 1995; Ofman et al. 1995; Chae et al. 1998; Patsourakos et al. 2002; Chae et al. 2002; Li & Habbal 2003; Nigro et al. 2004; Buchlin & Velli 2006; Neill & Li 2005; Parenti et al. 2006). These effects are not included in our model, and therefore the predicted nonthermal velocities must be treated as *lower* limits.

3. BASE MODEL RESULTS

Results for the base model are presented in Figure 1, which shows the evolution of velocity, temperature, and density at a position halfway up the leg of the strand. The conditions at this location are representative of the coronal section. Temperature rises rapidly during the nanoflare to a maximum of nearly 10 MK at the strand apex. This leads to a strong thermal conduction flux into the chromosphere, which drives a high-speed evaporative upflow (e.g., Antiochos & Sturrock 1978; Antiochos & Krall 1979; Doschek et al. 1982; Cheng et al. 1983; Fisher et al. 1985; Nagai & Emslie 1986; Antonucci et al. 1987; Peres et al. 1987; Mariska et al. 1989; Peres & Reale 1993; Hori et al. 1998; Patsourakos et al. 2004a; Warren & Doschek 2005). The upflow reaches a maximum speed of approximately 200 km s^{-1} near the end of the nanoflare at $t = 250$ s and then diminishes rather quickly as the plasma cools.

Density increases as the strand fills with plasma. The maximum density occurs at $t \approx 900$ s, well after the maxima in temperature and velocity. From this time on, the strand cools more gradually, primarily by radiation, and material slowly drains and condenses back onto the chromosphere.

The oscillations apparent in Figure 1 occur when the initial upflows in both legs collide at the top of the strand and rebound downward. Waves are generated that propagate back and forth

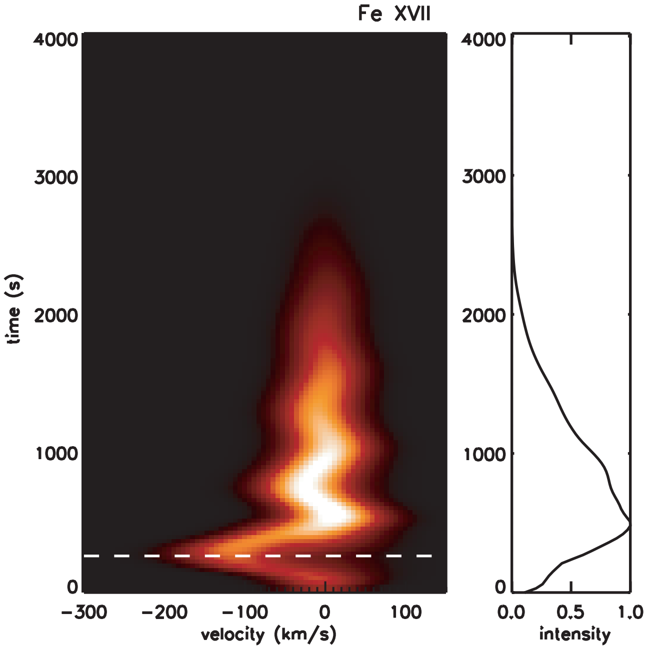

FIG. 2.—*Left:* Evolution of the Fe XVII profile for the coronal section of the base model. The square root of intensity is plotted as a function of wavelength (*horizontal axis*) and time (*vertical axis*). Wavelength is given in velocity units, with negative velocities corresponding to upflows and blueshifts. The dashed line indicates the end of the nanoflare. *Right:* Evolution of the profile-integrated Fe XVII intensity (normalized). [*See the electronic edition of the Journal for a color version of this figure.*]

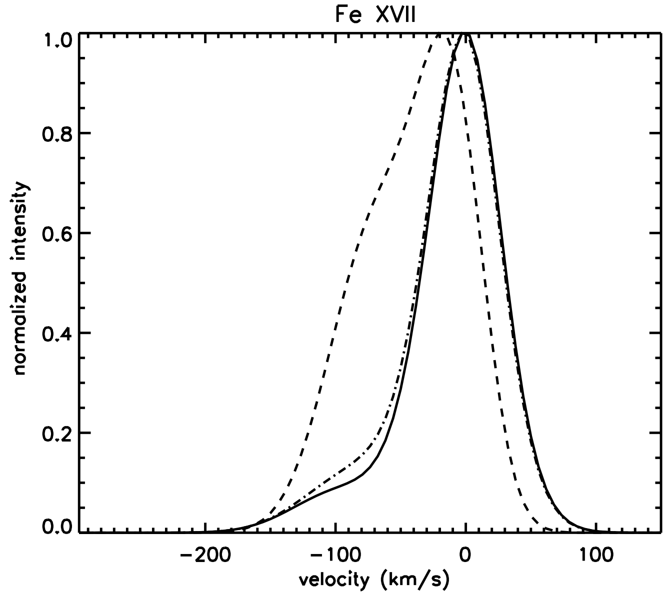

FIG. 3.—Normalized Fe XVII profiles averaged over the 4000 s duration of the base simulation, corresponding to a snapshot of a multistranded loop: the coronal section (*solid line*), the footpoint section (*dashed line*), and the entire loop (*dot-dashed line*). Negative velocities correspond to blueshifts (upflows). The corresponding thermal velocity calculated at the $T_{G_{\rm mean}}$ of Fe XVII is 40 km s^{-1}. The coronal profile has a nonthermal velocity of 36 km s^{-1} and a maximum intensity of 245 ergs cm^{-2} sr^{-1} s^{-1} Å^{-1} (for an assumed loop diameter of 3×10^8 cm). The footpoint profile is half as bright.

along the stand with a steadily diminishing amplitude. These have been seen in other simulations (e.g., Mendoza-Briceño et al. 2004; Nakariakov et al. 2004) and have been observed as oscillating Doppler shifts in hot emission lines (e.g., Wang et al. 2002).

3.1. Fe XVII (255 Å)

Figure 2 shows the evolution of the Fe XVII profile averaged over the coronal section of the strand. Intensity is represented by color, increasing from black to red to white. Wavelength (in velocity units) increases from left to right, and time increases from bottom to top. Each row in the display represents the line profile at a particular instant in time. The dashed line at 250 s marks the end of the nanoflare. The plot at the right shows the evolution of the total (profile-integrated) line intensity.

Flows are revealed in Figure 2 as Doppler shifts of the centroid of the profile. They form a bright "ridge" that deviates to the left for upflows (blueshifts) and to the right for downflows (redshifts). The initial high-speed upflows are clearly evident, as are the oscillations due to the rebound.

As indicated in equation (1), the intensity of the emission has a strong dependence on both temperature and density; density appears as a square, and $G(T)$ is sharply peaked for most lines. The initial rapid increase in brightness occurs partly because the plasma is heated to temperatures where Fe XVII is sensitive and partly because the density increases from evaporation. Peak intensity occurs at $t \approx 400$ s, when $G(T)$ and n are both close to their maxima. This is roughly 150 s after the time of greatest upflow velocity. The subsequent decrease in intensity is more gradual as the plasma cools through the temperature range of greatest sensitivity, as indicated by the dashed vertical lines in Figure 1. There is significant emission even after $G(T)$ drops below half-maximum, because density decreases relatively slowly. The intensity does not fall to 1/10 of its peak value until $t \approx 1800$ s.

As discussed in § 1, we envision that a coronal loop consists of a large number of unresolved strands at various stages of heating and cooling. To approximate a snapshot of such a loop, we average our single-strand simulation over the 4000 s duration of the run (the approximate nanoflare repetition time necessary to explain the observed coronal energy losses). This averaging is equivalent to vertically collapsing Figure 2 to obtain the single line profile that is shown in Figure 3 (*solid curve*). It approximates an observation of the coronal section of a multistranded loop. The profile is dominated by a "rest" component, because most of the emission is produced after the strongest evaporation, during the time of slow upflow and even slower downflow. There is nonetheless significant emission from the short interval of rapid upflow. This gives rise to a modest, yet distinctive enhancement in the blue wing of the profile. This spectral signature is an important prediction of our nanoflare model.

The dashed profile in Figure 3 represents the temporally averaged profile for the footpoint section of the loop. It has been normalized and is actually half as bright as the coronal profile. The footpoint is fainter because the transition region and low corona are too cool for Fe XVII, except during the short interval when the upper corona is extremely hot. This is when the fast upflows are occurring, so the centroid of the footpoint profile is significantly blueshifted.

It is unlikely that Fe XVII footpoint emission would be observed without confusion from overlying coronal emission. The dot-dashed profile in Figure 3 shows the more likely case of combined emission from the footpoint and coronal sections. The nonthermal velocities of the coronal, footpoint, and entire loop profiles are 36, 38, and 37 km s^{-1}, respectively, and are listed in Table 1.

The EIS instrument should have sufficient sensitivity and spectral resolution to discern the Fe XVII spectral features predicted by our model. Using the preflight instrument response function (J. Mariska & A. Winebarger 2005, private communication) and

TABLE 1

Nonthermal Velocities (in km s^{-1}) for the Base Model

Ion	Corona	Footpoint	Entire Loop
Ne VIII	28	14	19
Mg X	20	12	16
Fe XVII	36	38	37

assuming a loop diameter of 3000 km, comparable to what is typically observed by the *Transition Region and Coronal Explorer* (*TRACE*; e.g., Watko & Klimchuk 2000; Aschwanden & Nightingale 2005; López Fuentes et al. 2006), we predict a count rate of approximately 40 counts s^{-1} pixel^{-1} in the center of the coronal profile. The count rate will be less if the loop is only partially filled with nanoflare-heated strands. EIS has a spectral resolution of approximately 20 mÅ, which corresponds to a Doppler shift of approximately 30 km s^{-1} and is adequate to resolve the blue wing enhancement.

We remind the reader that the profiles in Figure 3 apply strictly to a semicircular loop lying in a vertical plane observed at disk center. Different shapes, orientations, and positions will produce different results. For example, if the loop plane is inclined relative to the line of sight (e.g., a tipped loop at disk center or a vertical loop near the limb), then the profile will be more narrow and the wing enhancement will occur at a smaller blueshift. A loop with a north-south baseline that is observed near the limb can have either blue wing enhancements in both legs or red wing enhancements in both legs, depending on whether the loop is tipped toward or away from the observer. A flat loop (not well rounded) with an east-west baseline that is observed near the limb will have a blue wing enhancement from the far leg and a red wing enhancement from the near leg. Thus, depending on the shape, orientation, and position of the loop, any combination of blueshift and redshift enhancements is possible. Moreover, the loop length can influence the hydrodynamic response of a loop to nanoflares (e.g., the thermal conduction flux that drives chromospheric evaporation is $\propto 1/L$). Detailed comparisons of models and observations will therefore require geometrical information from either magnetic field extrapolations or stereoscopic reconstructions (e.g., from the EUVI instrument on the *Solar Terrestrial Relations Observatory* [*STEREO*] mission).

We note that our simulated emission assumes ionization equilibrium, which is not always a good assumption when the plasma is evolving rapidly (e.g., Bradshaw & Mason 2003). We checked the validity of this assumption by calculating Fe XVII ionization times, $\tau_{\rm ion}$, and recombination times, $\tau_{\rm recomb}$, using atomic data provided by M. Laming (2005, private communication). These are shown in Figure 4, together with the temperature and temperature timescale, $\tau_{\rm temp} = T/|dT/dt|$, at a position halfway up the strand leg (the same location as in Fig. 1). For ionization equilibrium to be valid during the heating phase, $\tau_{\rm ion}$ must be smaller than $\tau_{\rm temp}$. This is the case in all but the first 40 s. For ionization equilibrium to be valid during the cooling phase, $\tau_{\rm recomb}$ must be smaller than $\tau_{\rm temp}$. This is also the case, except for a brief instant near $t = 220$ s. We conclude that the results for our base model are not significantly impacted by ionization nonequilibrium effects. This is also true for the Mg X and Ne VIII results discussed in §§ 3.2 and 3.3. Nonequilibrium effects will be more important in models 5 and 6, which begin with a much lower density. The early phase of high-speed evaporation in those models is especially vulnerable. The precise impact on the Fe XVII profile is unclear, and a simulation that properly accounts for these effects is being planned.

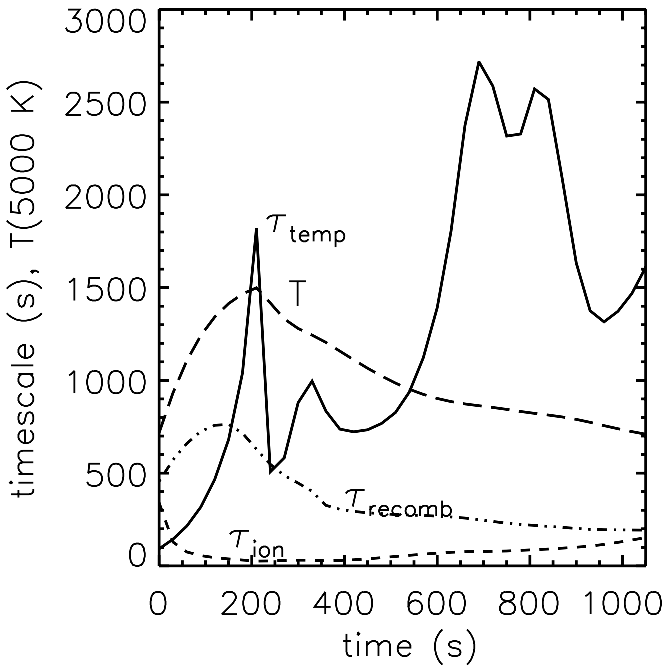

Fig. 4.—Evolution of important timescales halfway up the leg of the strand in the base model: Fe XVII ionization time (*short-dashed line*), Fe XVII recombination time (*double-dot–dashed line*), temperature timescale $T/|dT/dt|$ (*solid line*), and temperature (*long-dashed line*).

3.2. Mg X (625 Å)

Figure 5 shows the evolution of the Mg X profile for the coronal section of the strand in a format identical to that of Figure 2. The intensity increases very slowly and, in contrast to that of Fe XVII, is negligible during the time that evaporation is occurring. Peak intensity is not until $t \approx 3200$ s, near the end of the simulation. This behavior is mostly related to the temperature evolution. The plasma is much too hot for Mg X until long after the nanoflare has ended. Figure 6 shows the time-averaged coronal profile (*solid line*). It is symmetric, narrow, and very slightly redshifted, because it is produced primarily during the slow draining phase.

The footpoint profile (Fig. 6, *dashed line*) is very similar to the coronal profile. Even the amplitudes are comparable. This contrasts with the situation for Fe XVII, where the footpoint is only half as bright as the corona. The reason for this difference is that the transition region emits in Fe XVII only during the earliest part of the simulation, when the apex temperature is above about 6 MK, but it emits in Mg X for a much longer period, when the apex temperature is above about 2 MK. Some Mg X footpoint emission is produced during the evaporation phase, but since $I \propto P^2 T_a^{-7/2}$ during this phase (Appendix A), relatively little of it comes from the fastest upflows, when P is small and T_a is large. Furthermore, the upflows are slower in Mg X than in Fe XVII, because velocity scales with temperature for a constant mass flux at constant pressure. Very little of the Mg X footpoint emission is strongly blueshifted as a consequence. The nonthermal velocities of the coronal, footpoint, and entire loop profiles of Mg X are 20, 12, and 16 km s^{-1}, respectively.

3.3. Ne VIII (770 Å)

The time-averaged profiles for Ne VIII are shown in Figure 7. Much of our discussion of Mg X applies also to this line. Coronal emission becomes significant long after the nanoflare has occurred, when the plasma has cooled to a temperature where Ne VIII is

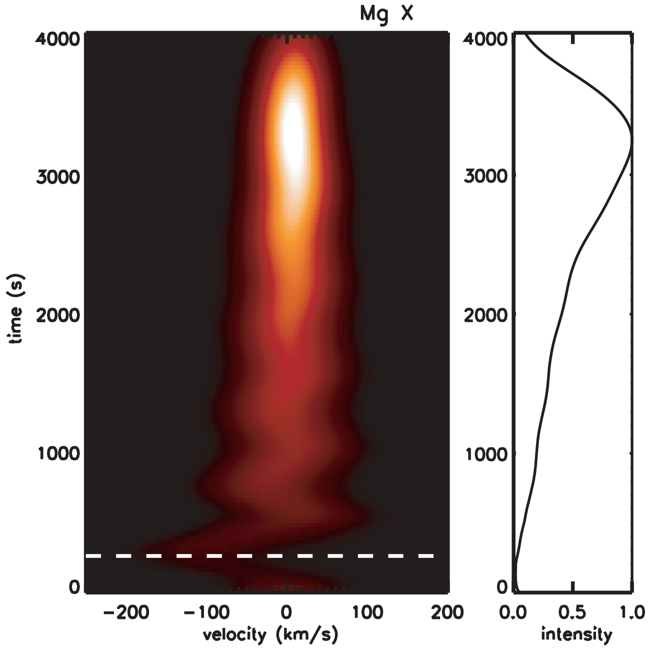

FIG. 5.—Same as Fig. 2, but for the Mg x line. [*See the electronic edition of the Journal for a color version of this figure.*]

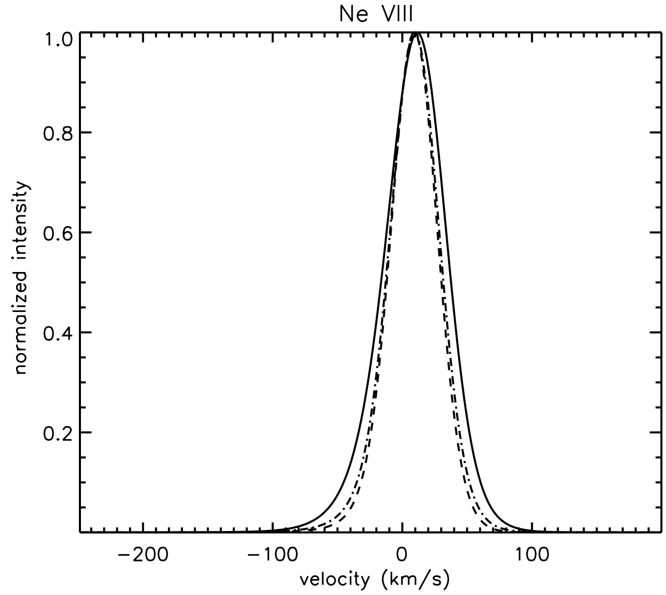

FIG. 7.—Same as Fig. 3, but for the Ne viii line. The amplitude of the coronal profile is 0.25 times that of the footpoint profile. The corresponding thermal velocity calculated at the $T_{G_{\rm mean}}$ of Ne viii is 20 km s^{-1}. The coronal profile has a nonthermal velocity of 28 km s^{-1}.

reasonably sensitive. Even at the end of the simulation, most of the corona is hotter than the temperature of peak $G(T)$. For this reason, the coronal profile (*solid line*) is about 4 times fainter than the footpoint profile (*dashed line*).

The nonthermal velocities of the coronal, footpoint, and entire loop profiles of Ne viii are 28, 14, and 19 km s^{-1}, respectively. It may seem odd that the nonthermal broadening of the coronal profile is appreciably larger for Ne viii than it is for Mg x. The reason is that the value of $T_{G_{\rm mean}}$ used in equation (1) underestimates the actual temperature of the emitting plasma to a greater extent for Ne viii than for Mg x. Recall that the corona is still too hot for Ne viii even at the end of the simulation. Since the true thermal broadening is larger than assumed, the nonthermal ξ that we compute is artificially large.

In a related study to ours, Spadaro et al. (2006) recently studied the Ne viii and Mg x lines, among others, using simulations of impulsively heated loops. However, since their goal was to explain the redshifts and shape of the differential emission measure distribution in the transition region, they used much shorter loops ($L = 5$–10 Mm) and much less energetic nanoflares that produce peak temperatures of $\sim$1 MK. They did not consider the nonthermal broadening of the lines.

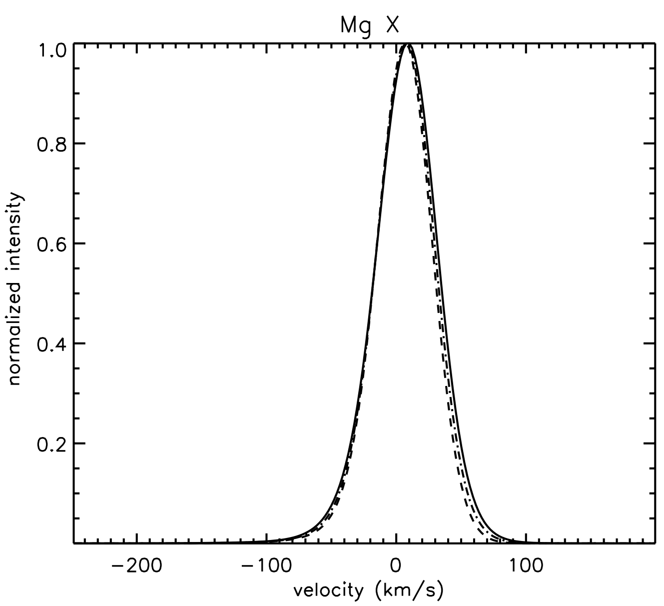

FIG. 6.—Same as Fig. 3, but for the Mg x line. The amplitude of the coronal profile is 0.97 times that of the footpoint profile. The corresponding thermal velocity calculated at the $T_{G_{\rm mean}}$ of Mg x is 24 km s^{-1}. The coronal profile has a nonthermal velocity of 20 km s^{-1}.

4. MODEL PARAMETER VARIATION

We now discuss the impact of varying different parameters of the base model. The details of the alternate models are listed in Table 2, and the corresponding Fe xvii nonthermal velocities are given in Table 3. Model 1 is the base model. Our discussion concentrates on the coronal profile of Fe xvii, since it is the one most sensitive to the model parameters. The Mg x coronal profile is discussed briefly in § 4.8.

4.1. *Nanoflare Energy*

Model 2 is identical to the base model, except that the heating rate and total energy of the nanoflare are 3 times larger. Figure 8 shows the Fe xvii coronal profile for this model, averaged over the duration of the simulation. The blue wing feature that is clearly evident in Figure 3 has largely disappeared. Some enhancement is present, but it is much fainter and extends to larger blueshifts. The nonthermal velocity of this profile is 30 km s^{-1}, which is significantly smaller than what we found for the base model.

These differences can be understood in terms of the velocity, temperature, and density evolution that is shown in Figure 9. As in Figure 1, the plotted values are from a position halfway up the strand leg. The threefold increase in the nanoflare energy produces higher temperatures and velocities, as discussed in Appendices B and C. As in the base model, T and v both peak near the end of the nanoflare, but because the peak temperature is higher than in the

TABLE 2
MODEL PARAMETERS

Model	L (Mm)	T_{0a} (MK)	$Q_{\rm nano}$ (ergs cm^{-3} s^{-1})	$\tau_{\rm nano}$ (s)	Spatial Dependence	Viscosity
1	150	2.5	0.01	250	Uniform	No
2	150	2.5	0.03	250	Uniform	No
3	150	2.5	0.05	50	Uniform	No
4	150	2.5	0.01	250	Footpoint concentration	No
5	150	0.5	0.0009	250	Uniform	No
6	150	0.5	0.0009	250	Uniform	Yes
7	60	2.5	0.07	250	Uniform	No

NOTE.—Definitions: L is the full length of the coronal semicircle, T_{0a} is the initial apex temperature, $Q_{\rm nano}$ is the nanoflare heating rate averaged along the strand, and $\tau_{\rm nano}$ is the nanoflare duration.

base model, it takes longer for the plasma to cool into the range of strong Fe XVII sensitivity. By this time, the upflows have slowed dramatically. The emission from the fastest upflows is strongly blueshifted, but it is very faint because the plasma is much too hot for Fe XVII. We might say that Fe XVII is better "tuned" to the evaporating plasma in the base model than it is in model 2.

4.2. *Nanoflare Duration*

Model 3 considers a much shorter nanoflare. The duration is only 50 s, which is 5 times shorter than in the base model, but the heating rate is 5 times larger, so the total nanoflare energy is the same. The Fe XVII wing enhancement is somewhat fainter and extends to slightly greater blueshifts compared to the base model, as shown in Figure 10. Depositing the nanoflare energy over a shorter period of time produces a slightly higher peak temperature, even with the same total energy, because there is less time for conductive cooling to act. The upflows are correspondingly faster. The consequences for Fe XVII emission are similar to what they are in model 2, but much less pronounced. The nonthermal velocity of 40 km s^{-1} is slightly larger than that in the base model.

4.3. *Nanoflare Spatial Distribution*

Model 4 uses the same spatially averaged heating rate as in the base model, but it is concentrated near the footpoints. The heating rate is 7.5 times greater at the top of the chromosphere and decreases exponentially above it with a scale length of 10 Mm. The total energy input is the same. Figure 11 shows that the blue wing enhancement is more pronounced than in the base model. There is a local intensity peak at approximately 150 km s^{-1} that might be described as a secondary component, distinct from the dominant rest component. As discussed in Patsourakos & Klimchuk (2005), an exponential heating profile like the one here produces hotter temperatures in the lower legs, but a cooler apex temperature compared to uniform heating. This gives rise to a stronger heat flux into the chromosphere and a faster evaporation, while at the same time creating coronal temperatures that are well tuned to Fe XVII.

4.4. *Initial Conditions*

In model 5, we explore the consequences of having smaller initial temperatures and densities, corresponding either to a much weaker level of steady background heating or to a longer delay between successive nanoflares. The beginning apex values are $T_{0a} = 0.5$ MK and $n_{0a} = 7 \times 10^6$ cm^{-3}. The apex density is reduced much more than the apex temperature for two reasons. First, the average density along a strand in static equilibrium scales roughly as temperature squared. Second, there is much more density stratification at the lower temperature because of the smaller gravitational scale height. In the base model, the gravitational scale height is more than double the strand height, but in model 5, it is only about half of the strand height. As discussed in Appendix B, a

TABLE 3
Fe XVII NONTHERMAL VELOCITIES FOR THE VARIOUS MODELS

Model	Nonthermal Velocity (km s^{-1})
1	36
2	30
3	39
4	Double component
5	Double component
6	Double component
7	19
Model 1 off limb	27

NOTE.—We do not measure the nonthermal velocities for profiles with double components.

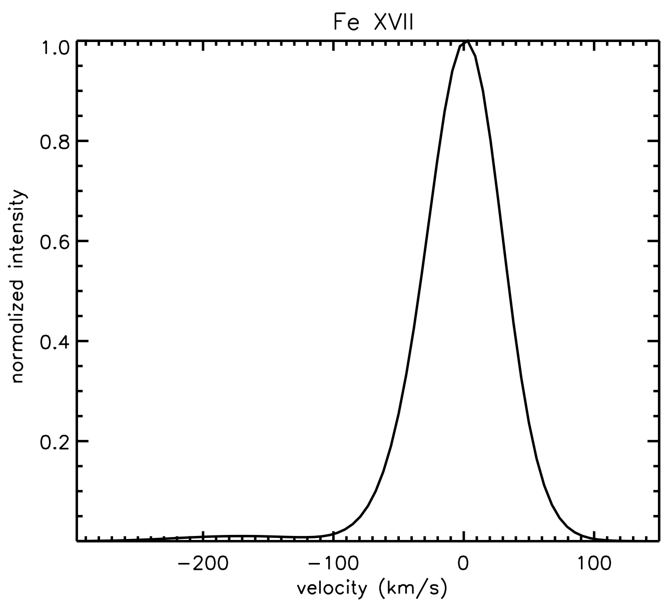

FIG. 8.—Fe XVII coronal profile for model 2, in which the nanoflare energy is 3 times larger than in the base model. The maximum intensity is 990 ergs cm^{-2} sr^{-1} s^{-1} Å^{-1} (for an assumed loop diameter of 3×10^8 cm), and the nonthermal velocity is 30 km s^{-1}.

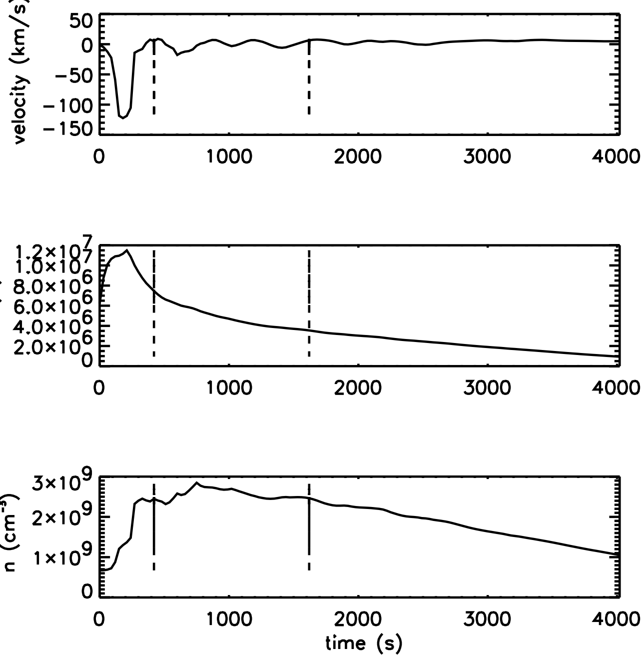

FIG. 9.—Same as Fig. 1, but for model 2, in which the nanoflare energy is 3 times larger than in the base model.

nanoflare with the energy of the base model would heat the low-density plasma to much higher temperatures than in the base model. We therefore use a smaller nanoflare that produces a peak temperature of about 10 MK.

The resulting Fe XVII profile, shown in Figure 12, has a very distinctive blueshift component centered near 210 km s^{-1}. The much faster upflows compared to the base model are due to the much smaller initial densities, as indicated by equation (C1). Because Fe XVII is well tuned to the temperature of the upflows, the intensity ratio of the blueshift to rest components is larger than in the other models. However, the total line intensity is less, because the densities are reduced throughout the simulation. We estimate that integration times of order 100 s would be necessary to obtain a reasonable observation. Note that ionization and recombination times are longer at lower densities, so a significant fraction of the blueshifted emission may be out of ionization equilibrium. A simulation that fully accounts for these effects is planned.

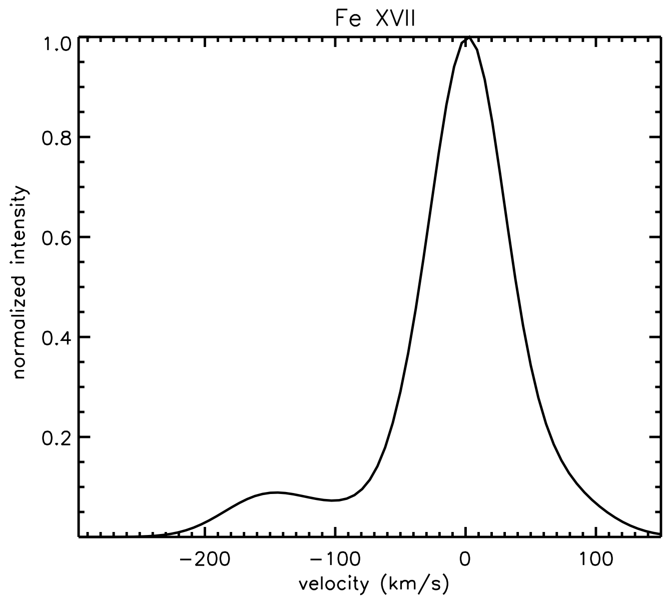

FIG. 11.—Fe XVII coronal profile for model 4, which is similar to the base model except that the nanoflare heating is concentrated near the footpoints. The maximum intensity is 210 ergs cm^{-2} sr^{-1} s^{-1} Å^{-1}.

4.5. *Compressive Viscosity*

The evaporative upflows in model 5 are fast enough to be supersonic, even at the elevated temperatures. Two propagating shock fronts develop at the top of the stand, where high-speed material from both legs collides and accumulates in a high-density plug. This seen in Figure 13, where the solid curves show the instantaneous temperature, density, and velocity as a function

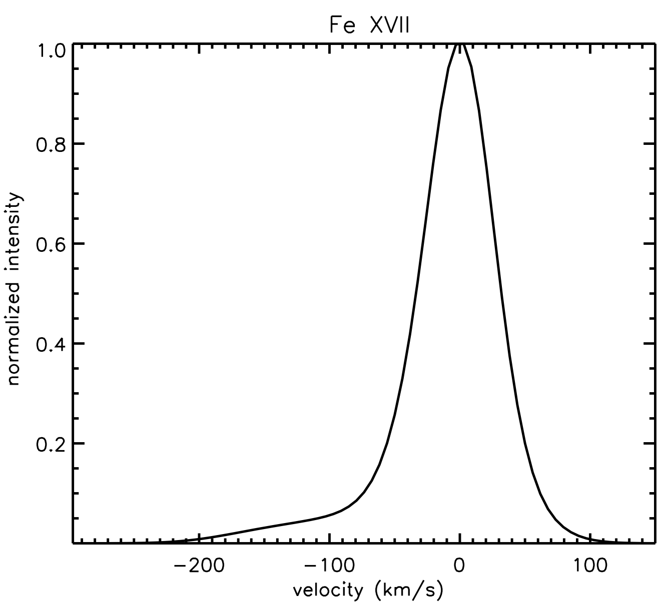

FIG. 10.—Fe XVII coronal profile for model 3, in which the nanoflare duration is 5 times shorter and the heating rate is 5 times larger than in the base model. The total nanoflare energy is the same. The maximum intensity is 250 ergs cm^{-2} sr^{-1} s^{-1} Å^{-1}, and the nonthermal velocity is 39 km s^{-1}.

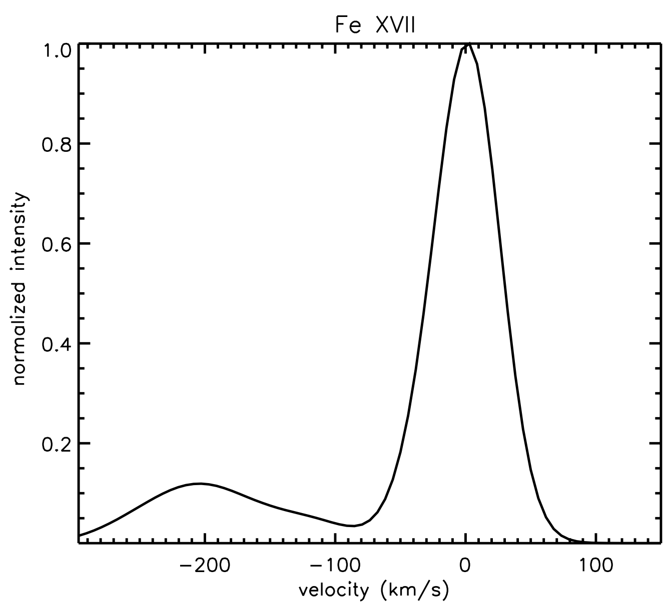

FIG. 12.—Fe XVII coronal profile for model 5, which is similar to the base model except that the initial temperature and density are much smaller. The maximum intensity is 0.37 ergs cm^{-2} sr^{-1} s^{-1} Å^{-1}.

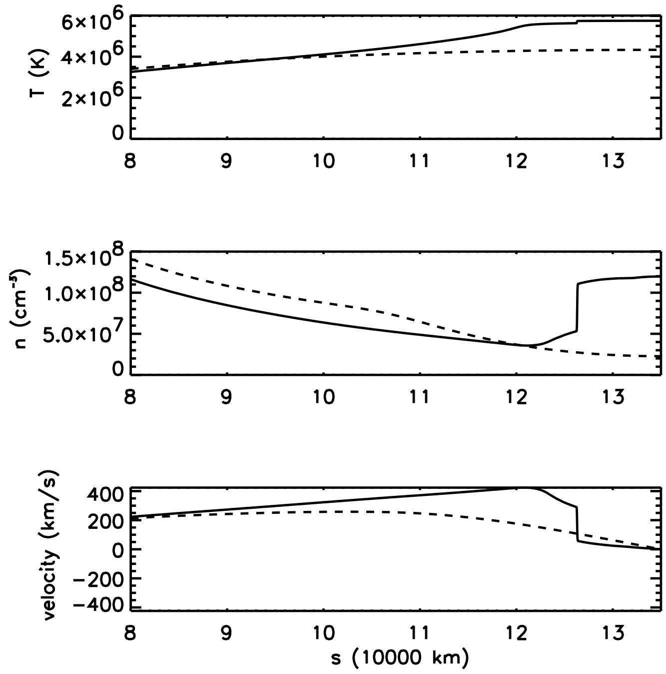

FIG. 13.—Temperature (*top*), density (*middle*), and velocity (*bottom*) vs. position along the strand shortly after the end of the nanoflare ($t = 270$ s) for model 5 (*solid curves*), which does not include compressive viscosity, and for model 6 (*dashed curves*), which does. All other aspects of the models are the same. The strand apex is at the right edge of the plot.

of position along the strand shortly after the end of the nanoflare ($t = 270$ s). The top of the strand is at the right edge of the plot, and the chromosphere is off the left edge, near $s = 6$ Mm. The shock is clearly visible at $s = 12.7$ Mm.

Compressive viscosity can be important in regions of steep temperature gradient, such as shocks, especially when the temperatures are high and the densities are low. The Reynolds number at the shock in Figure 13 is only of order 10^{-2}, so viscosity, which is not included in the simulation, would be expected to have a major smoothing effect. Furthermore, the electron mean free path is $\lambda_{\rm mfp} = 7 \times 10^3 T^2/n \sim 10^9$ cm throughout much of the corona in model 5, so our fluid description breaks down near the shock. We have therefore repeated the simulation and included compressive viscosity. Model 6 is identical to model 5, except that a viscous force term, $\mu(\partial/\partial s)(\partial v/\partial s)$, is added to the momentum equation and a viscous heating term, $\mu(\partial v/\partial s)^2$, is added to the energy equation, where $\mu = 10^{-16} T^{5/2}$ g^{-1} s^{-1} is the coefficient of compressive viscosity under coronal conditions (Spitzer 1962). The dashed curves in Figure 13 show the resulting change in the temperature, density, and velocity. The shock is entirely smoothed out. Peres & Reale (1993) found a similar result in their study of full-size flares. Like us, they computed synthetic line profiles, but they considered hotter lines of Ca XIX and Fe XXV that are appropriate to 20 MK flares.

The presence of viscosity modifies the Fe XVII profile, as shown in Figure 14. The blueshift component is slightly slower, but the main difference is its increased intensity relative to the rest component. This is due to both an increase in the brightness of the blueshift component and a decrease in the brightness of the rest component. Most of the rest emission in models 5 and 6 comes from the top of the strand, where the Doppler shifts are reduced because of the slower velocities and because the strand is more horizontal and therefore more misaligned with the viewing direction. Figure 15 shows how the time-averaged emission varies along the strand. The format is similar to Figure 2, except

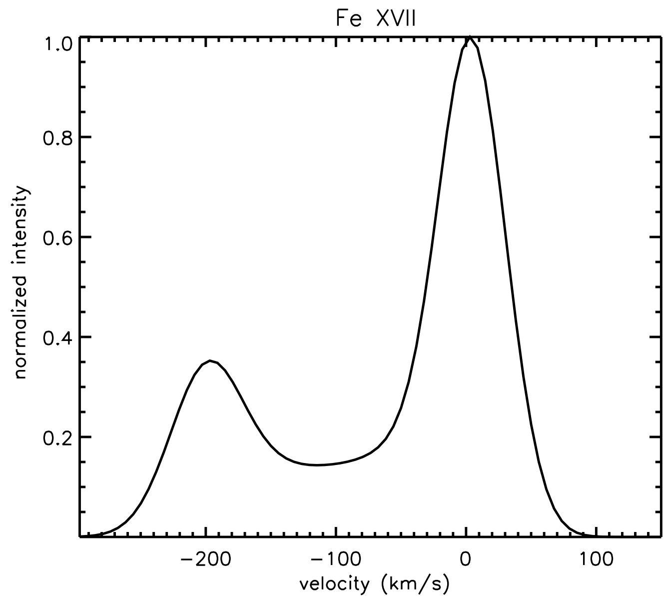

FIG. 14.—Fe XVII coronal profile for model 6, which is similar to model 5 except that compressive viscosity is included. The maximum intensity is 0.13 ergs cm^{-2} sr^{-1} s^{-1} Å^{-1}.

that the vertical axis indicates position rather than time. The brightest emission originates near the strand apex, at the top of the display. The apex emission is even brighter in model 5 than what is shown here for model 6, because of the high-density plug of accumulating material.

It is important to note that compressive viscosity would not be significant in our base model, where the evaporative upflows are

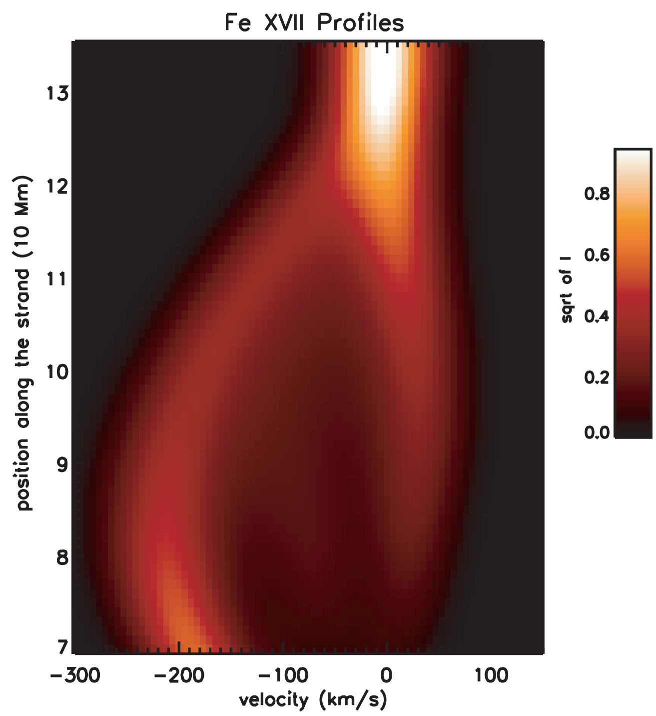

FIG. 15.—Time-averaged Fe XVII profiles as a function of position along the coronal section of the strand for model 6, which includes compressive viscosity. The square root of intensity is plotted as a function of wavelength (*horizontal axis*) and location (*vertical axis*). The apex is at the top. The wavelength is given in velocity units, with negative velocities corresponding to upflows and blueshifts. [*See the electronic edition of the Journal for a color version of this figure*.]

subsonic and do not form shocks. This was verified with a simulation that includes viscosity.

4.6. *Strand Length*

Model 7 has a coronal semicircle that is only 60 Mm long, 2.5 times shorter than that in the base model. This length is typical of observed SXR loops (e.g., Kano & Tsuneta 1995; Porter & Klimchuk 1995). We use prenanoflare and nanoflare heating rates that produce initial and maximum apex temperatures of $\approx$2.5 and 10 MK, respectively, similar to those of the base model. The Fe XVII coronal profile for model 7 has a blue wing enhancement with similar velocity to that of the base model, but a considerably weaker intensity relative to the rest component. The similar velocities are expected on the basis of equation (C4). The reason for the different relative intensities is not so obvious. One is tempted to conclude that it is related to differences in the durations of the conduction and radiation phases, which produce the wing and rest emission, respectively. Equation (D2) indicates that, for the same values of T_{0a} and T_a, the conductive cooling time and thus the duration of the evaporation phase scale linearly with L (see Appendix D). A shorter loop will have a shorter evaporation phase. However, using reasoning similar to that in Cargill (1993), it can be shown that the radiation phase also scales linearly with L, so it too should be shorter for a shorter loop. The two effects would cancel, and the ratio of the wing and rest intensities would be similar. Perhaps the difference that is seen in models 1 and 7 is due to the fact that T_{0a} and T_a are not exactly the same in the two models.

Since the total cooling time is relatively short in model 7, it is reasonable to consider time averages that are less than the 4000 s we have used for the other models. A 1000 s average produces a maximum intensity of 10,000 ergs cm^{-2} sr^{-1} s^{-1} Å^{-1} for an assumed loop diameter of 3×10^8 cm. The higher densities of this simulation give rise to smaller ionization and recombination times than for the base simulation, which guarantees ionization equilibrium conditions. The nonthermal velocity of the profile is 19 km s^{-1}.

4.7. *Observing Geometry*

As we have discussed, the shape of the line profile depends on the observing geometry (i.e., the shape of the loop and its orientation with respect to the line of sight). We therefore calculated how the Fe XVII profile would appear if the base model were located at the limb with an east-west alignment. The profile is perfectly symmetric and has minimal blue wing and red wing enhancements. The fastest velocities are in the lower legs of the loop, but they are now nearly orthogonal to the line of sight and are not significantly Doppler-shifted. The top portion of the loop is well aligned with the observing direction, but the velocities are much slower. The nonthermal velocity is only 27 km s^{-1}, and the maximum intensity is 254 ergs cm^{-2} sr^{-1} s^{-1} Å^{-1} for an assumed loop diameter of 3×10^8 cm.

4.8. Mg X *Profiles*

The Mg X profiles for models 2–7 are similar to the Mg X profile for the base model. As for the base model, all of the profiles are narrow and do not exhibit any significant blue wing enhancement. The nonthermal velocities lie in the range of 12–30 km s^{-1}.

5. OBSERVATIONS

With this work we calculated for the first time the nonthermal velocities predicted by nanoflare heating occurring at subresolution strands that collectively make up the observed coronal loops. We calculated profiles for three representative spectral lines formed at cool, warm, and hot temperatures: Ne VIII (770 Å), Mg X (625 Å), and Fe XVII (255 Å).

A large number of the Ne VIII and Mg X observations give nonthermal velocities of $\approx$15–30 and 10–38 km s^{-1}, respectively (e.g., Hassler et al. 1990; Chae et al. 1998; Teriaca et al. 1999; Erdélyi et al. 1998; Doschek & Feldman 2000; Peter 2001; Landi et al. 2003; E. Landi 2004, private communication). The observed profiles do not exhibit any significant asymmetries. The observations were mainly made by the Solar Ultraviolet Measurement of Emitted Radiation (SUMER, on *SOHO*) with a spatial resolution of $\approx 1''$ in quiet-Sun and active regions both on disk and off-limb locations, with few of them corresponding to some averaging in space (e.g., along the slit or the observed two-dimensional field). Our simulations are broadly consistent with the observations: they predict nonthermal velocities just as much as what is observed, and the simulated profiles do not exhibit asymmetries, which is again in line with the observations.

SUMER observations by Landi et al. (2003) and Feldman et al. (2003) of hot lines give nonthermal velocities of $\approx$20–40 km s^{-1} in the temperature range of $\approx$2.6–6.6 MK, which partially overlaps with the temperature range of Fe XVII formation. The observations were carried out in two flaring active regions during periods of quiescence, well before or after the occurrence of flares. The SUMER slit was fixed at off-limb locations, meaning that one-dimensional distributions (along the slit) of the nonthermal velocities were obtained.

The magnitude of the observed nonthermal broadening can be certainly reproduced by the model of § 4.7, which corresponds to a limb observation. Moreover, the above observations show that the profiles are not characterized by appreciable asymmetries, which is again in agreement with the symmetric profile discussed in § 4.7.

SXR observations of quiescent active regions in the disk with coarse ($\approx 15''$) and no spatial resolution made by the Bent Crystal Spectrometer (BCS) on the *Solar Maximum Mission* (*SMM*) and by *Yohkoh*, respectively, gave nonthermal velocities in the range of $\approx$40–50 km s^{-1} for temperatures of $\approx$3 and 5 MK (Saba & Strong 1991; Sterling 1997). Few of our simulations (e.g., the base simulation) can reproduce the magnitude of the observed nonthermal velocities. The coarse spectral resolution of these observations (for example, the spectral resolution of the Sterling 1997 observations was $\approx$110 km s^{-1}) was not probably adequate to detect line profile asymmetries of the magnitude predicted by our models.

The ability of our models to reproduce the magnitude of the observed line broadening for cool, warm, and hot lines leads us to conclude that nanoflares are able to account for the observed nonthermal broadening. Our models also lead to symmetric profiles for the cool and warm lines, as is observed. They can also lead to symmetric profiles in hot lines for off-limb observations, which is in agreement with the observations. Moreover, the nanoflare model produces more line broadening for hot lines than for cool lines, as is observed. Our results therefore provide new and significant pieces of evidence in favor of nanoflares as the heating agent of multistranded coronal loops.

There has been some concern that the high-speed upflows, often reaching several hundred km s^{-1}, that are associated with chromospheric evaporation could lead to extremely large line widths and blueshifted components that overwhelm the near-stationary emission (e.g., Hori et al. 1998; Doschek 2002; Feldman et al. 2004; Phillips et al. 2005; Warren & Doschek 2005). Our modeling clearly demonstrates that this is not the case. The emission from a single strand can be highly blueshifted during a small part of its evolution, but the composite emission from many strands in various stages of heating and cooling is dominated by near-stationary emission. Subresolution structuring can also be the key to reproducing the spectral signatures of flaring loops, as compared to single-stranded loop models (e.g., Hori et al. 1998; Warren & Doschek 2005).

The mass motions that produce the nonthermal velocities in our simulations are a response to the nanoflare energy input, which we assume to take the form of a simple heating of the plasma. In reality, the nanoflare event may also directly accelerate the plasma. This would be the case for MHD processes such as magnetic reconnection, for example, which can produce plasma jets at the local Alfvén speed of $\approx$1000 km s^{-1} under typical coronal conditions. The ability of our simulations to reproduce the magnitude of the observed nonthermal velocities suggests that such jets are not important contributors to the line broadening. Klimchuk (1998) argued on independent grounds that the emission measure of hot, high-velocity reconnection jets should be very low and therefore they would escape detection. If the emission measure were large, the predicted line broadening would be far greater than what is observed (Cargill 1996).

Finally, we note that most published measurements of nonthermal velocities, especially those from hot lines, are based on observations that are averaged over large areas or that lack two-dimensional information. These areas undoubtedly encompass several loops, and the loops could have significantly different properties. The strongest possible test of the nanoflare model requires observations of individual loops in fully two-dimensional spatial fields. Such observations should be possible with EIS.

6. SUMMARY AND RECOMMENDATIONS

We have investigated the spectral line profiles and nonthermal broadening expected from loops that are bundles of unresolved, impulsively heated strands. We obtained several important results. First, spectral lines with formation temperatures characteristic of the transition region (e.g., Ne VII, formed near 0.7 MK) and the warm corona (e.g., Mg X, formed near 1.3 MK) are predicted to have modest broadening and minimal enhancement of the wings of the line. These predictions are very consistent with actual observations. While this is not strong evidence that the nanoflare model is correct, since there are other possible sources of modest line broadening, it is a critical test that the model has passed.

A second important result is that hot lines (e.g., Fe XVII, formed near 5 MK) are predicted to sometimes have appreciable broadening and distinctive enhancements in the line wings. This is generally consistent with existing observations, but observations of hot lines are quite limited, so no strong conclusions can be drawn at this time. We anxiously await the launch of *Solar-B* and its EIS spectrometer, which should provide a more rigorous test of the model.

We found that the Fe XVII profiles depend on a number of different parameters, including the magnitude and duration of the nanoflare, the distribution of the nanoflare heating along the loop strand, and the conditions in the strand before the nanoflare occurs. This is both good news and bad news. It is good in that there is the potential of using line profile observations to diagnose the properties of the nanoflares. This would be extremely valuable for guiding our thinking on the physical nature of nanoflares and for testing coronal heating theories (Klimchuk 2006). It is bad news in that we must sort out several competing effects. Observations in multiple hot lines are extremely important in this regard. We have found that wing emission signatures of nanoflares depend sensitively on whether the spectral line is well "tuned" to the temperature of the fast evaporative upflows. With multiple lines covering a range of temperatures, it should be possible to pinpoint the temperature and velocity of the upflows and thereby to more easily infer the properties of the energy release. EIS will observe lines of Fe XXI, formed at 10 MK, and Fe XXIII, formed at 16 MK, in addition to Fe XVII.

Future progress will require several improvements to our present study. Detailed and accurate predictions of line profiles are possible only if the three-dimensional shape of the loop is known. Such information can in principle be obtained from magnetic field extrapolations based on photospheric magnetograms or from stereoscopic loop observations such as those expected from the upcoming *STEREO* mission. Improved predictions must also account for ionization nonequilibrium effects and for compressive viscosity, especially in cases where the prenanoflare densities are very low. These modeling improvements are all straightforward and, when combined with spectroscopic observations having high spectral and spatial resolution and comprehensive temperature coverage, should provide definitive answers. EIS will be a big step in this direction, but a next-generation imaging spectrometer should be a high priority for the future.

This research was supported by NASA and ONR. We thank Spiro Antiochos, Judy Karpen, and George Doschek for useful discussions, Martin Laming for providing atomic data, Enrico Landi for providing unpublished SUMER data, and John Mariska and Amy Winebarger for providing EIS response functions. Sincere thanks go to the referee, Fabio Reale, for very constructive comments and criticism.

APPENDIX A

TRANSITION REGION LINE INTENSITY

The intensity of a spectral line formed near temperature T in the transition region is given approximately by

$$I \propto n^2 \frac{T}{|dT/ds|}. \tag{A1}$$

If we assume that the thermal conduction flux is approximately constant through the transition region during times of strong evaporation, then

$$F_c \propto T^{5/2} \frac{dT}{ds} \sim \frac{2}{7} \frac{T_a^{7/2}}{L}, \tag{A2}$$

where T_a is the apex temperature and L is the loop half-length. Combining these equations, we get

$$I \propto n^2 T_a^{-7/2} \propto P^2 T_a^{-7/2} \tag{A3}$$

for a given spectral line (i.e., a given transition region temperature). A more rigorous derivation shows that the dependence on the apex temperature is actually closer to $T_a^{-5/2}$. In any case, there is a strong inverse dependence on T_a.

APPENDIX B

APEX TEMPERATURE

For nanoflares that are significantly shorter than the radiative cooling timescale (>10^4 s), the radiation energy losses can be ignored, and most of the input energy goes into raising the thermal energy density of the plasma, which is proportional to pressure. If the nanoflare is also shorter than the conductive cooling timescale (which is equal to the evaporation timescale, ~500 s), then density is approximately constant, and the apex temperature increases in proportion to the nanoflare energy:

$$T_a \propto \frac{E_{\rm nano}}{LAn_{0a}}, \tag{B1}$$

where $E_{\rm nano}$ is the nanoflare energy, A is the strand cross-sectional area, and n_{0a} is the initial (prenanoflare) apex density. If the nanoflare heating rate is extreme, the apex temperature may increase to a point where thermal conduction becomes important and limits a further temperature rise. In that case, equation (B1) overestimates the peak apex temperature. Nonetheless, the peak apex temperature is always greater for larger nanoflares, shorter strands, and lower initial densities.

APPENDIX C

EVAPORATION VELOCITY

During periods of strong evaporation, the thermal conduction flux powers the enthalpy flux of the evaporated plasma:

$$n_0 T v \propto \frac{T_a^{7/2}}{L}, \tag{C1}$$

where v is the evaporation velocity at temperature T in the low corona. We have assumed here that the density is approximately uniform in the low corona and is equal to its initial value, n_0. Equation (C1) shows that higher apex temperatures and smaller densities produce faster upflows as observed in a given spectral line (i.e., at a given temperature). Combining with equation (B1) and assuming that the strand is not short compared to a gravitational scale height, so that $n_{0a} \approx n_0$, we get

$$v \propto \frac{E_{\rm nano}^{7/2}}{(n_{0a}L)^{9/2}}. \tag{C2}$$

Larger nanoflares, shorter lengths, and lower initial densities give rise to faster upflows. Note that L in these expressions will be smaller than the loop half-length if the nanoflare heating is concentrated near the footpoints. Note also that the velocity in equations (C1) and (C2) will be reduced if thermal conduction cannot be ignored during the nanoflare heating.

In static equilibrium,

$$T_{0a} \propto (n_{0a}L)^{1/2} \tag{C3}$$

for a radiative loss function that varies as $T^{-1/2}$. Equation (C1) can then be rewritten as

$$v \propto \frac{T_a^{7/2}}{T_{0a}^2}\frac{1}{T}, \tag{C4}$$

where we have again assumed that $n_{0a} \approx n_0$. The evaporation velocity observed in a given spectral line is largely independent of strand length for all models with the same initial and maximum apex temperatures.

APPENDIX D

CONDUCTIVE COOLING TIME

The thermal conduction cooling time that indicates the rate of temperature decrease during strong evaporation is given by

$$\tau_{\text{cond}} \propto \frac{n_{0a}L^2}{T_a^{5/2}}. \tag{D1}$$

Using equation (C3), we get

$$\tau_{\text{cond}} \propto \frac{T_{0a}^2}{T_a^{5/2}}L. \tag{D2}$$

For the same initial and maximum apex temperatures, the cooling time is proportional to the strand length.

REFERENCES

Antiochos, S. K., & Krall, K. R. 1979, ApJ, 229, 788
Antiochos, S. K., MacNeice, P. J., Spicer, D. S., & Klimchuk, J. A. 1999, ApJ, 512, 985
Antiochos, S. K., & Sturrock, P. A. 1978, ApJ, 220, 1137
Antonucci, E., et al. 1987, ApJ, 322, 522
Aschwanden, M. J., Newmark, J. S., Delaboudinère, J. P., Neupert, W. M., Klimchuk, J. A., Gary, G. A., Portier-Fornazzi, F., & Zucker, A. 1999, ApJ, 515, 842
Aschwanden, M. J., & Nightingale, R. W. 2005, ApJ, 633, 499
Aschwanden, M. J., Nightingale, R. W., & Alexander, D. 2000, ApJ, 541, 1059
Ayres, T. R., Brown, A., Harper, G. M., Osten, R. A., Linsky, J. L., Wood, B. E., & Redfield, S. 2003, ApJ, 583, 963
Boland, B. C., et al. 1975, MNRAS, 171, 697
Bradshaw, S. J., & Mason, H. E. 2003, A&A, 401, 699
Brosius, J. W., Thomas, R. J., Davila, J. M., & Landi, E. 2000, ApJ, 543, 1016
Buchlin, É., & Velli, M. 2006, ApJ, submitted
Cargill, P. J. 1993, Sol. Phys., 147, 263
———. 1994, ApJ, 422, 381
———. 1996, Sol. Phys., 167, 267
———. 2004, ApJ, 605, 911
Cargill, P. J., Mariska, J. T., & Antiochos, S. K. 1995, ApJ, 439, 1034
Chae, J., Poland, A. I., & Aschwanden, M. J. 2002, ApJ, 581, 726
Chae, J., Schuhle, U., & Lemaire, P. 1998, ApJ, 505, 957
Cheng, C.-C., Doschek, G. A., & Feldman, U. 1979, ApJ, 227, 1037
Cheng, C.-C., Oran, E. S., Doschek, G. A., Boris, J. P., & Mariska, J. T. 1983, ApJ, 265, 1090
Chung, S. M., Drake, J. J., Kashyap, V. L., Lin, L. W., & Ratzlaff, P. W. 2004, ApJ, 606, 1184
Dahlburg, R. B., Klimchuk, J. A., & Antiochos, S. K. 2003, Adv. Space Res., 32, 1029
———. 2005, ApJ, 622, 1191
Dere, K. P., Landi, E., Mason, H. E., Monsignori Fossi, B. C., & Young, P. R. 1997, A&AS, 125, 149
Dere, K. P., & Mason, H. E. 1993, Sol. Phys., 144, 217
Doschek, G. A. 2002, in ASP Conf. Ser. 277, Stellar Coronae in the *Chandra* and *XMM-Newton* Era, ed. F. Favata & J. J. Drake (San Francisco: ASP), 89
Doschek, G. A., Boris, J. P., Cheng, C.-C., Mariska, J. T., & Oran, E. S. 1982, ApJ, 258, 373
Doschek, G. A., & Feldman, U. 2000, ApJ, 529, 599
Doyle, J. G., O'Shea, E., Erdélyi, R., Dere, K. P., Socker, D. G., & Keenan, F. P. 1997, Sol. Phys., 173, 243
Erdélyi, R., Doyle, J. G., Perez, M. E., & Wilhelm, K. 1998, A&A, 337, 287
Feldman, U., Dammasch, I., Landi, E., & Doschek, G. A. 2004, ApJ, 609, 439
Feldman, U., Landi, E., & Curdt, W. 2003, ApJ, 585, 1087
Fisher, G. H., Canfield, R. C., & McClymont, A. N. 1985, ApJ, 289, 414
Hassler, D. M., Rottman, G. J., Shoub, E. C., & Holtzer, T. E. 1990, ApJ, 348, L77
Hori, K., Yokoyama, T., Kosugi, T., & Shibata, K. 1998, ApJ, 500, 492
Inverarity, G. W., Priest, E. R., & Heyvaerts, J. 1995, A&A, 293, 913
Kano, R., & Tsuneta, S. 1995, ApJ, 454, 934
Karpen, J. T., Antiochos, S. K., Hohensee, M., Klimchuk, J. A., & MacNeice, P. J. 2001, ApJ, 553, L85
Karpen, J. T., & Devore, C. R. 1987, ApJ, 320, 904
Kjeldseth Moe, O., & Nicolas, K. R. 1977, ApJ, 211, 579
Klimchuk, J. A. 1998, in Solar Jets and Coronal Plumes, ed. T.-D. Guyenne (ESA SP-421; Noordwijk: ESA), 233
———. 2000, Sol. Phys., 193, 53
———. 2006, Sol. Phys., 234, 41
Klimchuk, J. A., & Cargill, P. J. 2001, ApJ, 553, 440
Kopp, R. A., & Poletto, G. 1993, ApJ, 418, 496
Landi, E., Feldman, U., Innes, D. E., & Curdt, W. 2003, ApJ, 582, 506
Lenz, D. D., DeLuca, E. E., Golub, L., Rosner, R., & Bookbinder, J. A. 1999, ApJ, 517, L155
Li, X., & Habbal, S. R. 2003, ApJ, 598, L125
López Fuentes, M. C., Klimchuk, J. A., & DéMoulin, P. 2006, ApJ, 639, 459
Mariska, J. T., & Boris, J. P. 1983, ApJ, 267, 409
Mariska, J. T., Emslie, A. G., & Li, P. 1989, ApJ, 341, 1067
Marsch, E., Wiegelmann, T., & Xia, L. D. 2004, A&A, 428, 629
Mendoza-Briceño, C. A., Erdélyi, R., & Sigalotti, L. Di G. 2002, ApJ, 579, L49
———. 2004, ApJ, 605, 493
Müller, D. A. N., Peter, H., & Hansteen, V. H. 2004, A&A, 424, 289
Nagai, F., & Emslie, A. G. 1984, ApJ, 279, 896
Nakariakov, V. M., Tsiklauri, D., Kelly, A., Arber, T. D., & Aschwanden, M. J. 2004, A&A, 414, L25
Nigro, G., Malara, F., Carbone, V., & Veltri, P. 2004, Phys. Rev. Lett., 92, 194501
Ofman, L., Davila, J. M., & Steinolfson, R. S. 1995, ApJ, 444, 471
O'Neill, I., & Li, X. 2005, A&A, 435, 1159
Pallavicini, R., Peres, G., Serio, S., Vaiana, G., Acton, L., Leibacher, J., & Rosner, R. 1983, ApJ, 270, 270
Parker, E. N. 1983, ApJ, 264, 642
———. 1988, ApJ, 330, 474
Parenti, S., et al. 2006, ApJ, in press
Patsourakos, S., Antiochos, S. K., & Klimchuk, J. A. 2004a, ApJ, 614, 1022
Patsourakos, S., Habbal, S. R., & Hu, Y. Q. 2002, ApJ, 581, L125
Patsourakos, S., & Klimchuk, J. A. 2005, ApJ, 628, 1023
Patsourakos, S., Klimchuk, J. A., & MacNeice, P. J. 2004b, ApJ, 603, 322
Patsourakos, S., & Vial, J.-C. 2000, A&A, 359, L1
Peres, G., & Reale, F. 1993, A&A, 267, 566
Peres, G., Reale, F., Serio, S., & Pallavicini, R. 1987, ApJ, 312, 895
Peter, H. 1999, ApJ, 516, 490
———. 2001, A&A, 374, 1108
Phillips, K. J. H., Feldman, U., & Harra, L. K. 2005, ApJ, 634, 641
Porter, L. J., & Klimchuk, J. A. 1995, ApJ, 454, 499
Redfield, S., Ayres, T. R., Linsky, J. L., Ake, T. B., Dupree, A. K., Robinson, R. D., & Young, P. R. 2003, ApJ, 585, 993
Rosner, R., Tucker, W. H., & Vaiana, G. S. 1978, ApJ, 220, 643
Saba, J. L. R., & Strong, K. T. 1991, ApJ, 375, 789
Schmitt, J. H. M. M., & Wichmann, R. 2001, Nature, 412, 508
Serio, S., Peres, G., Vaiana, G. S., Golub, L., & Rosner, R. 1981, ApJ, 243, 288
Serio, S., Reale, F., Jakimiec, J., Sylwester, B., & Sylwester, J. 1991, A&A, 241, 197
Singh, J., Ichimoto, K., Sakurai, T., & Muneer, S. 2003, ApJ, 585, 516
Spadaro, D., Lanza, A. F., Karpen, J. T., & Antiochos, S. K. 2006, ApJ, 642, 579
Spadaro, D., Lanzafame, A. C., Consoli, L., Marsch, E., Brooks, D. H., & Lang, J. 2000, A&A, 359, 716
Spitzer, L. 1962, The Physics of Fully Ionized Gases (2nd ed.; New York: Interscience)

Sterling, A. C. 1997, ApJ, 478, 807
Teriaca, L., Banerjee, D., & Doyle, J. G. 1999, A&A, 349, 636
Testa, P., Peres, G., & Reale, F. 2005, ApJ, 622, 695
Walsh, R. W., Bell, G. E., & Hood, A. W. 1997, Sol. Phys., 171, 81
Wang, T. J., Solanki, S. K., Curdt, W., Innes, D. E., & Dammasch, I. E. 2002, ApJ, 574, L101
Warren, H. P., & Doschek, G. A. 2005, ApJ, 618, L157
Watko, J. A., & Klimchuk, J. A. 2000, Sol. Phys., 193, 77
Winebarger, A. R., & Warren, H. P. 2004, ApJ, 610, L129
Winebarger, A. R., Warren, H. P., & Mariska, J. T. 2003, ApJ, 587, 439
Withbroe, G. L., & Noyes, R. W. 1977, ARA&A, 15, 363
Young, P. R., Del Zanna, G., Landi, E., Dere, K. P., Mason, H. E., & Landini, M. 2003, ApJS, 144, 135
Young, P. R., Dupree, A. K., Wood, B. E., Redfield, S., Linsky, J. L., Ake, T. B., & Moos, H. W. 2001, ApJ, 555, L121
Zirker, J. B. 1993, Sol. Phys., 147, 47